Impact driving of monopiles in centrifuge: effect on the lateral response in sand

Semaan Maatouk, Matthieu Blanc, Luc Thorel

Impact driving of monopiles in centrifuge: effect on the lateral response in sand

Semaan Maatouk[1]
PhD candidate, Laboratory of Centrifuges for Geotechnics, Department GERS, Gustave Eiffel University, Bouguenais, France (Orcid:0000-0003-2125-1020)

Matthieu Blanc[2]
Researcher, Laboratory of Centrifuges for Geotechnics, Department GERS, Gustave Eiffel University, Bouguenais, France (Orcid:0000-0003-0603-487X)

Luc Thorel[3]
Senior researcher, Laboratory of Centrifuges for Geotechnics, Department GERS, Gustave Eiffel University, Bouguenais, France (Orcid:0000-0002-0218-4144)

Corresponding author: semaan.maatouk@univ-eiffel.fr, +33 2 40 84 59 15

Submitted: 10/05/2021

Accepted: 28/07/2021

Number of words: 5736

Number of figures: 10

Number of tables: 7

Ahead of print in International Journal of Physical Modelling in Geotechnics, Ice Publishing. Published online : 06/09/2021
https://doi.org/10.1680/jphmg.21.00035

Abstract

This study examines the influence of impact-driven installation on the subsequent horizontal monotonic response of small-scale monopiles by using a large-beam geotechnical centrifuge at 100*g*. A special device including small-scale hammer was developed to install open-ended monopiles with 50 mm in diameter to an embedment depth of 250 mm in flight, and then to apply lateral loading on the monopile head without stopping the centrifuge. The horizontal global and local responses of the monopiles were investigated for two methods of installation: impact driven at 100*g,* and monotonically jacked at 1*g* into saturated dense sand. The results highlighted two main features. (i) The effect of impact driving was pronounced for small amplitudes of horizontal loading. With regard to the conditions of serviceability, the in-flight installation increased the secant stiffness by about 3 times compared with the 1*g* installation. For large amplitude of displacement, the lateral capacity increased by 1.3 times. (ii) The experimental *p*-*y* curves obtained from the in-flight impact-driven installation remained smoother than those predicted by using offshore standards, but were similar to them.

Keywords: centrifuge modelling; pile and piling; sand

Notation

C_u	coefficient of uniformity [dimensionless]
D	monopile outer diameter [m]
d_{50}	average diameter of sand grains [mm]
EI	monopile bending stiffness [N m^2]
G	monopile shear modulus [GPa]
g	Earth gravitational acceleration [m/s^2]
H	horizontal load [MN]
H_G	horizontal load at the ground level [MN]
h	ram drop height [m]
h_a	anvil height [m]
k	lateral secant stiffness
L	monopile embedment length [m]
l	monopile length [m]
l_e	load eccentricity [m]
M	bending moment [MN m]
M_G	bending moment at ground level [MN m]

m	ram mass [kg]
N	g level [dimensionless]
n	hammer blows [dimensionless]
p	soil reaction [MN/m]
R_N	radius of the application of the Centrifuge acceleration [m]
S	shear force [MN]
s	monopile settlement [m]
s_i	monopile settlement for the hammer impact n° i [m]
t	monopile wall thickness [m]
y	monopile lateral deflection [m]
y_G	monopile lateral deflection at ground level [m]
z	depth coordinate [m]
ε	monopile normal strain [µm/m]
ϵ	energy delivered to drive the monopile [MJ]
Φ	angle of friction [°]
θ	rotation of monopile neutral axis [°]
θ_G	rotation of monopile neutral axis at ground level [°]
κ	Timoshenko shear coefficient [dimensionless]
ξ	applied cumulated driving energy [MJ]
ξ^N	simplified cumulated driving energy [MJ]
ρ_{dmax}	maximum dry density [g/cm^3]
ρ_{dmin}	minimum dry density [g/cm^3]
ρ_s	dry density of solid particles [g/cm^3]
Δ	improvement of the monopile resistance/secant stiffness [%]

1 Introduction

Offshore wind farms have grown in number in the last few decades in the course of efforts to produce clean and renewable energy. Monopiles are the prevalent foundations for offshore wind turbines in shallow coastal waters (e.g. Dupla *et al*., 2019). They are commonly installed in dense sand using a dynamic method: the so-called impact driving. Over their design service life, the monopiles are subjected to horizontal loading due to winds, currents, and waves. This is why offshore monopiles are designed to withstand lateral loads and overturning moments.

To investigate the lateral response of impact-driven monopiles in sandy environments, two experimental methods have been proposed in the literature: in-situ testing and laboratory testing. Field tests can be performed onshore on monopiles of different sizes. For example, monotonic lateral tests were conducted on driven monopiles of small-to-medium diameters (0.273–2 m) under the framework of the Pile Soil Analysis (PISA) joint industry project (McAdam *et al*., 2020; Burd *et al*., 2020a). Small-scale model tests have been conducted in laboratories, either at 1*g* (e.g. Abadie *et al*., 2019) or with enhanced stress, by accelerating the centrifuge (e.g. Klinkvort, 2012 ; Fan *et al*., 2019). Centrifuge models tested in macro-gravity undergo similar stress fields to full-scale prototypes. Hence, by using the scaling laws of physical modelling (e.g. Garnier *et al*., 2007), the response of the monopile model can be compared to that of the prototype. Like the in-situ conditions, the method of installation (e.g. for displacement or non-displacement piles) plays an important role on the pile behaviour. The generated stress field changes significantly depending on the method of pile installation used: whether driven or wished in place. In the same way in the centrifuge, the stress field generated during installation at 1*g* is different from that when installation is performed in flight. The horizontal response of the model of the pile obtained through the centrifuge is weaker than that predicted by standards such as the DNVGL (2016) (e.g. Bayton and Black (2016), Choo and Kim (2016), El Haffar (2018)). One reason for this is that clean sand is used in centrifuge modelling, and is significantly different than that used in situ. Another reason, reported by Fan *et al*. (2019), is that driving the monopile in flight increases the stiffness of the horizontal response as well as the lateral resistance of soil. As highlighted by Bayton and Black (2016), the experimental response of the monopile in this case is expected to be closer to the design standards. A miniature monopile-driving hammer can thus be developed to simulate the method of ‘in-flight’ installation during centrifuge model tests. The three main characteristics of hammering are its frequency (blow rate), the mass of the ram, and the drop height. A list of different in-flight hammers developed to drive piles and monopiles in centrifuges (updated from Levacher *et al.*, 2008) is provided in Table 1.

Several studies have focused on the lateral responses of piles and monopiles installed in the centrifuge by using different methods. Kim *et al.* (2004) have highlighted different lateral responses of piles installed as wished in place, and by being driven at 1*g* by using different energies. Furthermore, Dyson and Randolph (2001), and Klinkvort (2012) have studied the effects of monotonically jacked and impact-driven in-flight installations on the responses of the lateral pile and the monopile. However, these tests required stopping the centrifuge to mount the lateral loading apparatus, which led to a loss of the state of soil post installation. Fan *et al*. (2021a) showed by using advanced numerical modelling that the post-installation state of soil, including horizontal stresses and the void ratio, is altered by the process of installation of the monopile in dry and sandy environments. The post-installation state of soil therefore needs to be retained in centrifuge modelling. This was achieved by Fan *et al*. (2019), who performed three direct monotonic push-over tests without stopping the centrifuge on a 50-mm monopile model monotonically jacked at 1*g* and 100*g,* and impact-driven at 100*g* into dry sand of medium density to a depth of 3.1*D*. Fan *et al*. (2019) claimed that the global lateral response of the monopile was significantly influenced by the method of installation, and this was numerically confirmed by Fan *et al*. (2021b). Fan *et al*. (2021b) also revealed that the effect of the method of installation on the lateral response is affected by the initial density of soil, driving distance, geometry of the monopile, and the level of stress and eccentricity of the load.

This study develops an experimental device that can carry out, in centrifuge at 100g, the impact-driven installation of an instrumented monopile with 50 mm in diameter into a 250 mm (5*D*) embedding, followed by horizontal loading. Test was conducted to verify the performance of the set-up, and to better understand the effect of the impact-driven installation of the monopile on its subsequent global and local lateral response in saturated dense sand.

2 Development of the experimental device

To study the influence of the hammering installation method in centrifuge on the horizontal response of the monopile, a special device was developed. The goal of development was to drive the monopile in flight and then apply horizontal loading without stopping the centrifuge to maintain the states of stress that had been induced by the installation of the monopile beforehand. This enabled the better modelling of the post-installation stress field. The device (Figure 1) had two main axes. (i) Vertically, an electric motor was fixed at the top on a hydraulic actuator; it was positioned on I-shaped supporting beams, and was used to control the hammer (shown in Figure 2(a)). (ii) Horizontally, an electro-mechanical actuator was fixed on a 'T-metallic' support beam to laterally load the monopile. These actuators were equipped with external force sensors and displacement sensors (Table 2). The electro-mechanical hammer was based on the principle of the combined spin-upward movement of the ram before free-fall.

A 0.166-kg steel anvil was fixed over the head of the aluminium monopile to avoid damaging it at the moment of shock. The falling mass included wing-shaped ram weights, and two diametrically opposed cylinder bearings were wrapped around them. These two bearings rested on a fixed wave-shaped ram support that allowed the ram to free-fall to a height of 25 mm to hit the anvil and then move back up the ram with a constant slope through rotation. The shape of the ram support thus enabled the impact driving of the monopile with two blows per turn. The ram support, driving guide, and housing of the hammer were supported by the vertical actuator to follow the descent of the monopile. Inside the hollow rod of the hydraulic actuator, a connection bar that linked the vertical fork to the electric motor enabled its rotation. This rotating fork allowed for both the vertical translation (rise up and free-fall) and rotation of the free ram. The details of the miniature hammer are presented in Figure 2(b).

As the monopile penetrated the soil, the vertical actuator followed it downward while maintaining a specified drop height for impact through a vertical laser displacement transducer (Table 2) that measured the distance to the target fixed on the monopile shaft (as shown in Figure 2(a)). A driving guide fixed below the hammer also ensured the verticality of the monopile during installation. During the hammering, the monopile slightly spun about its vertical axis. This was avoided by using a steel rod that diametrically crossed the monopile 25 mm from its head and hung on the foot of the driving guide. A slight gap was provided between the hole of the monopile and the steel rod to avoid excessive pressure from being generated inside the monopile during hammering.

Once the monopile had reached the desired embedment depth, the electric motor spinning the ram was stopped. The vertical actuator was then lifted up to leave the monopile inside the sand sample. The possible translation and rotation of the monopile after installation in the vertical plan of the horizontal loading were measured by using two horizontal laser displacement transducers positioned in front of the horizontal actuator (Figure 2(a)). A maximum slight translation of 1 mm and rotation of 0.57° were observed in the direction opposite to that of the lateral loading.

Following this, without stopping the centrifuge to maintain the stress state, lateral loading was applied to the centre of the cross-section of the monopile by pushing the steel rod that crossed the monopile perpendicularly to the direction of loading by using a fork attached to the horizontal electro-mechanical actuator. A photograph of the horizontal loading set-up after unloading the monopile and stopping the centrifuge is presented in Figure 3.

The hydraulic vertical actuator, horizontal electric actuator, and electric motor were together connected to a MOOG© test controller placed near the axis of the centrifuge. The controller contained three servo-loops working at a frequency of up to 1.6 kHz that could be connected to various types of sensor (force, displacement, and acceleration).

3 Centrifuge model test

The tests were performed in a geotechnical centrifuge facility, with a beam of radius 5.5 m, at the Gustave Eiffel University, Nantes campus, France (formerly IFSTTAR or LCPC). The set-up was installed in the swinging basket of the centrifuge (Figure 1(b)), where the total available vertical height was 2110 mm. The tests were carried out at 100 times the Earth's gravity (N =100) on a large monopile model of diameter D = 50 mm embedded over 5D into water-saturated dense sand, and was horizontally loaded at an altitude of l_e = 5D from the ground level. The level of g was applied at a depth of 83 mm from the surface of soil (i.e. L/3), corresponding to a radius R_N of 5.2 m from the axis of the centrifuge.

3.1 Sand model

The sand sample was reconstituted by using the raining deposition technique (Garnier, 2001), which yields a homogenous specimen and has good repeatability (Ternet, 1999). Poorly graded NE34 Fontainebleau sand was deposited from an automatic hopper that moved back and forth at a constant horizontal speed of 10 cm/s. The sand fell at a constant height of 70 cm through a 3-mm-wide slot to produce uniform sand rain over a strongbox with internal dimensions of 1200 (length) by 800 (width) by 360 (depth) mm^3. The resulting density was 1.682 g/cm^3, with a coefficient of variation of 0.24%, i.e. 82% ± 1.4% of relative density, and was based on seven calibrated boxes spread at the bottom of the strongbox (C_u = 1.53, d_{50} = 0.21 mm, Φ = 38°, ρ_s = 2.65 g/cm^3, ρ_{dmin} = 1.434 g/cm^3, ρ_{dmax} = 1.746 g/cm^3 (Klinkvort, 2018)). Following the pluviation of sand, a 120-mm-high raiser (Figure 1) was placed over the strongbox. The sample was then saturated by tap water through vertical rising flow using four draining channels located at the bottom of the specimen (Figure 1(a)). To avoid scale effects between diffusion and the dynamic phenomena, the sand mass can be saturated by using a fluid with a viscosity of 100 cst (Kutter, 1994). This was not done in this study. Only the impact of the method of installation on the horizontal response of the monopile was studied here. The final water level was 40 mm above the surface of sand at 1g to ensure that the sand remained fully saturated at 100g. The effective unit weight of the saturated sand was 10.26 kN/m^3.

3.2 Monopile model

An open-ended tubular aluminium 2017A tube (Figure 4(a)) of length l = 525 mm, external diameter D = 50 mm, and a 2.5 mm-thick wall (t) was used. Two optical fibres, described below, were embedded into a tube of suitable thickness (thicker than the minimum thickness required according to API (2007)) while respecting the scale factor of flexural rigidity *EI*. Aluminium tubes are commonly used in geotechnical centrifuges (e.g. Rosquoët *et al*., 2007), and they do not rust in a saturated sand. The geometry and the mechanical characteristics of the model monopile are presented in Table 3.

The roughness of the pile, normalised by the average grain size as introduced by Uesugi and Kishida (1986), was 0.015 (less than 0.1). Therefore, it was considered to be smooth according to Garnier and Konig (1998), and the normalised surface roughness is typically within the range of 0.02 to 0.03 of a standard offshore pile, as reported De Nicola and Randolph (1997).

To avoid particle-size effect on the horizontal response of the monopile, a series of 'modelling of models' performed by Remaud (1999) have suggested a ratio of pile to grain diameter D/d_{50} greater than 60. In addition, the ratio of the thickness of the wall to mean particle size t/d_{50} needed to be at least 10 (De Nicola, 1996). Both criteria were verified (D/d_{50} = 238, t/d_{50} = 12) by using Fontainebleau NE34 sand and the geometry of the chosen monopile.

3.3 Monopile instrumentation

The model monopile was instrumented with two diametrically opposed optical fibres, each with a diameter of 200 µm, glued into two semi-cylindrical grooves with a radius of 0.5 mm (1/5 of the thickness of the wall) as shown in Figure 4(b). The position of the two optical fibres, in extension and compression sides, compensated for the effect of temperature on the resulting bending moment. Within each fibre, 10 equally distributed fibre Bragg gratings (FBGs) were integrated from the ground level to the pile base over a span of 225 mm, as shown in Figure 4(a). The details of this instrumented model monopile and its calibration have been provided by Li *et al*. (2020).

In an open-ended monopile, plugging may occur during installation to change the response. For this purpose, the internal height of the soil column during monopile installation was measured by using a potentiometric position sensor (Table 2) fixed by an aluminium support on the steel rod inside the monopile. The tip of the sensor rod was 160 mm from the monopile base before installation.

3.4 Hammering procedure

The monopile restricted within the driving guide penetrated a few millimetres into the sand before spinning the centrifuge, and then continued to penetrate into it as gravity was increased. At 100*g*, the displacement of the vertical hydraulic actuator holding the hammer was controlled to maintain the required height at which the ram was dropped based on the vertical displacement of the laser. The electric motor was then activated and impact driving was initiated. In general, the driving energy input into the system can be varied according to the drop height and the mass of the ram of the hammer. In this case, the ram weighed 0.164 kg, and a drop height of 20 mm was chosen.

The driving energy per stroke increased with the depth of penetration as the centrifugal acceleration varied with the radius (i.e. with the altitude of the anvil). Because the head of the anvil was located at an altitude corresponding to 88.65*g* before the monopile was driven, and at one corresponding to 92.84*g* at the end of the hammering, the delivered energy chosen to drive the model monopile down to the desired depth varied from 2.85 J to 2.99 J (2.85 MJ to 2.99 MJ at prototype scale, with N = 100). The maximum rotational speed of the electric motor was 900 rounds per minute, but it was fixed in this case to 150 rpm, which corresponded to five blows per second.

Figure 5 shows the cumulative number of blows of the hammer (n), the simplified cumulative driving energy ξ^N (without variation in the gradient of centrifuge acceleration during hammering), and the applied driving energy ξ (with variations) versus the normalised settlement of the monopile. In both cases, the driving energy (ϵ_{i+1}^N and $\epsilon_{\mathrm{i+1}}$) and the cumulative driving energy (ξ_{i+1}^N and $\xi_{\mathrm{i+1}}$) at the (i+1)th blow in 'MJ' were calculated at prototype scale as follows:

$$\begin{cases} \epsilon_{i+1}^N = mghN \\ \epsilon_{\mathrm{i+1}} = \epsilon_{i+1}^N \dfrac{R_{\mathrm{N}} - \dfrac{L}{3} - l - h_{\mathrm{a}} + s_{\mathrm{i}}}{R_{\mathrm{N}}} \end{cases} \tag{1}$$

$$\begin{cases} \xi_{i+1}^{N} = n_{i+1}\epsilon_{i+1}^{N} \\ \xi_{\mathrm{i+1}} = \xi_{\mathrm{i}} + \epsilon_{\mathrm{i+1}} \end{cases} \tag{2}$$

where all the length-related parameters were at model scale in 'm', and the height of the anvil h_a = 0.014 m. The initial depth s_0, around 0.65*D*, represented the monopile penetration under its own weight before being driven. The number of blows as well as the delivered energy required per unit meter of penetration increased with the penetration depth, as expected. A total of 3846 blows were needed to drive the monopile to an embedment depth of 5*D*. The maximum difference in cumulative energy between the methods of calculation was 12.8%. During this installation, the vertical displacement sensor inside the monopile indicated that no plugging had occurred.

3.5 Horizontal loading procedure

After installation, the hammer and the vertical actuator were lifted up in flight to create the required clearance around the head of the monopile for the lateral loading phase. Lateral loading was applied by pushing the steel rod, positioned perpendicularly with respect to the plane of the optical fibres at l_e = 250 mm (i.e. 5*D*), above the ground level. This was achieved by moving the horizontal electro-mechanical actuator to 50 mm (i.e. 1*D*) at a controlled rate of 0.1 mm/s. During the loading phase, the lateral load at the electro-mechanical actuator was recorded by using a horizontal load cell. The horizontal deflections of the monopile at 60 mm and at 220 mm above the ground level were measured by using two horizontal laser displacement transducers. These transducers, positioned in front of the actuator, were mounted on a bracket attached to the bottom of the I-beams (as shown in Figures 2(a) and 3).

The measurements of the sensors were recorded by a data acquisition system (QuantumX MX1615 from HBK) placed in the swinging basket of the centrifuge. The FS22DI Industrial BraggMETER Interrogator box from HBK, which can record the reflected peak wavelength in Bragg optical fibres to allow for the measurement of the normal strain, was placed near the axis of the centrifuge. These two data acquisition devices were connected to the same local ethernet network at a recording frequency of 100 Hz.

4 Impact of driving monopile on horizontal response

For comparison with the impact-driven installation (called 'ID100g' here), a reference monopile monotonically jacked at 1*g* (called 'J1g') was first tested in the same strongbox. The 1*g* installation was performed at a constant displacement rate of 1 mm/s to a depth of 5*D.* Then, centrifuge acceleration was applied at 100*g* only in the lateral loading phase (detailed in Section 3.5). As a result, the stress states of soil generated around the monopiles were different from those obtained after impact driving at 100*g*. Both tests were carried out at 8*D* (i.e. 400 mm) from the walls of the strongbox, perpendicular to the plane of horizontal loading, to minimise boundary-related issues. In this section, all results are presented at an equivalent prototype scale.

4.1 Comparison of global behaviour

Direct measurements of the ground-level displacement and rotation, and force are not feasible in the centrifuge. These data can be obtained by modelling the above-ground structure as a beam according to Timoshenko's theory (Astley (1992)) by using two displacement transducers positioned at different elevations (Mayall, 2019; Fan *et al*., 2019). However, this approach did not yield sufficiently accurate results for two reasons. i) There were uncertainties in displacements of small amplitude at the bottom laser displacement transducer (as shown in Figure 9). ii) The distance between these transducers was too short to yield accurate values of rotation. Moreover, the recommended use of inclinometers in field tests along the embedded depth (Burd *et al*., 2020a; Byrne *et al*., 2020; McAdam *et al*., 2020) was not possible in the centrifuge. This is why the procedure developed by Li *et al*. (2020) was implemented: The centre of rotation of the monopile was used to infer its horizontal displacement and rotation at the ground level. This method is detailed in the next sub-section as it involves strain measurements along the embedded depth of the monopile.

At ground level, the bending moment M_G and horizontal load H_G are plotted, in Figure 6(a) and Figure 6(b) respectively, against the rotation of the monopile about the neutral axis θ_G and its normalised deflection y_G/D for both methods of installation: by impact driving at 100*g* (ID100g), and monotonically jacked at 1*g* (J1g). In both tests, two trends/behaviours were observed. i) Initially, for small amplitudes of loading, the lateral resistance increased until θ_G = 0.7° or y_G = 0.03D (i.e. 0.15 m). ii) Then, this increase became less pronounced. For the same y_G/D or θ_G, H_G or M_G was always greater for ID100g than for J1g. Figure 6(a) and Figure 6(b) also show the improvement (Δ) brought about by the in-flight impact-driven installation. This improvement corresponded to the difference in the resistance of the monopile between the tests as normalised by the lateral resistance in the J1g test. The improvement due to the hammering was much more pronounced during the first phase of the tests (until θ_G = 0.7°). In the second phase, the difference between the resistance of the tests remained constant. As the resistance increased during loading, the improvement, due to the in-flight installation decreased until reaching a plateau for high amplitudes of loading far from the domain of serviceability. The findings are in accordance with the results obtained by Fan *et al*. (2019). To better understand these trends, authors focus on the local behaviour of the monopile instrumented by optical strain gauges.

4.2 Comparison of local behaviour

The resistance of the monopile to lateral loading depends on several mechanisms of interaction (Byrne *et al*., 2017): the horizontal soil reactions *p*, the interface shear along the monopile shaft, and the shear and moment resistances at its base.

4.2.1 Axial strains

Under lateral loading, the monopile bent to induce axial strains in optical fibres located at the extremities of the cross-section in the direction of loading. For both tests ID100g and J1g, these local strains as measured by FBGs are plotted in Figure 7 along the depth of the monopile for four loading states, corresponding to M_G = 100, 200, 300, and 400 MN.m. As the applied loading increased, normal strains within the monopile increased as well. Under the same value of M_G, normal strains in both tests increased with depth until reaching a maximum at the fourth FBG (z = 1.5D), below which they continued to decrease progressively to almost zero near the monopile base. However, the ID100g test featured amplitudes of axial strain lower than those of the J1g test. At the same depth, asymmetry was noted between compression and tension, and became more significant at the monopile base. This asymmetrical behaviour has been reported by Doherty *et al*. (2015) and McAdam *et al*. (2020) in lateral field tests on steel piles driven into dense sand. However, the reason for this was not identified. It may have occurred due to the localisation of strain along the boundaries of the monopile, as its slenderness ratio was too low to consider the monopile to be an ‘idealised flexible beam’.

4.2.2 Bending moments

After calibration of the FBGs (Li *et al*., 2020), bending moments at different depths of the monopile were calculated, as shown in Equation 3, based on the average values of the tensile and compressive strains ε_{avg} by using Euler–Bernoulli beam theory:

$$M = \frac{2EI\varepsilon_{avg}}{D} \tag{3}$$

To obtain the profile of the bending moment along the monopile, an interpolation of the moment calculated at each FBG level needed to be done. This was achieved by using fifth-order polynomial fitting, which provided the best estimate of the measured data. Six coefficients in the polynomial needed to be identified. The first three were determined from i) the bending moment calculated at the first FBG level (i.e. at the ground level), ii) the shear force at the ground surface calculated by dividing the zero-exponent coefficient by load eccentricity l_e, and iii) the absence of soil reaction at the ground surface. The remaining coefficients were determined from the best fit of the measured data presented as empty markers in Figure 8. Note that at the monopile tip, no boundary condition was considered. At the ground level in both tests, the maximum difference between the moment calculated by the FBG and that calculated by multiplying load eccentricity with loads measured by the horizontal load cell was less than 0.2%. This confirms the reliability of the FBGs used in this study. In both tests, J1g (Figure 8(a)) and ID100g (Figure 8(b)), the moment increased with the depth up to approximately 1.5D below the ground surface. Then, the moment gradually decreased to a very low value at 4.5D. However, the existence of a moment-related reaction at the monopile base is difficult to confirm.

4.2.3 Soil reactions

The first and second derivatives of the profiles of the bending moment yielded profiles of the shear force and the horizontal soil reaction if the distributed moment along the monopile shaft was negligible. Experimentally, this distributed moment was difficult to assess. However, authors neglected it here based on work by Burd *et al*. (2020b). They conducted numerical simulations similar to our tests in a saturated, dense, sandy medium by using a 1D finite element model (calibrated on a 3D FEM) with *L*/*D* = 6. They obtained a resistance lower than 7% when considering only the lateral soil reactions compared with when all mechanisms were considered. In this study, profiles of the shear force *S* and soil reaction *p* are plotted in Figure 8. For the same horizontal load, *S* and *p* were similar in both tests. ID100g featured higher lateral resistance than J1g.

4.2.4 Deflections

The monopile was modelled following Timoshenko's beam theory (i.e. shear strains within the monopile were included). The profiles of its neutral axis of rotation *θ* (clockwise positive) and deflection *y* were determined as follows:

$$\theta = -\frac{1}{EI}\int Mdz + \frac{S}{\kappa AG} - c_1 \tag{4}$$

$$y = \frac{1}{EI}\iint Mdz - \frac{M}{\kappa AG} + c_1 z + c_2 \tag{5}$$

where Timoshenko's shear coefficient *κ* was equal to 0.9 (Faghidian, 2017), *A* is cross-sectional area of the monopile, *G* is its shear modulus (see Table 3), and two integration constants c_1 and c_2 were obtained by using the monopile deflection measured by the top non-contact laser displacement transducer and the deflection of the monopile at its rotation centre. The latter was determined by finding the depth at which the soil reaction between two loading increments remained constant (El Haffar, 2018). At this depth, the horizontal displacement of the monopile remained constant between the two load increments.

Figure 8 also shows the normalised deflection of the monopile *y*/*D* and its neutral axis of rotation θ. In contrast to the profiles *S* and *p*, those of *y*/*D* and θ in ID100g were lower than in J1g. Figure 9 presents the normalised deflection profiles of the monopile above and below the ground surface for both tests at four loading states (for M_G every 100 MN.m until 400 MN.m). The depth at which no deflection was obtained corresponded to a distance of 18.75 m from the ground surface, i.e. *z*/*D* = 3.75 or z/L = 0.75. This depth was close to the centre of rotation of the monopile. The figure also shows monopile deflections measured by the bottom laser displacement transducer (not used for the integration procedure). These measurements were consistent with the deflection profiles obtained previously. The slight difference in case of the ID100g test was due to uncertainties captured in case of small displacements.

4.2.5 Load transfer curves

The influence of the method of installation on the *p*-*y* curves at different depths (between 0.5*D* and 3*D*) is shown in Figure 10. For small loading amplitudes, the *p*-*y* curves of the ID100g test had stiffer responses than those of the J1g test. This tendency became less pronounced with increasing loading. At the first level, *z* = 0.5*D,* the soil reactions reached the same plateau in both tests. At deeper layers, this was difficult to determine as not enough displacements were generated to reach a plateau.

The increase in the initial stiffness can be explained by an increase in horizontal stress along the monopile shaft during in-flight installation compared with that in case of a jacked monopile. Before the horizontal loading, the radial stress should be higher for ID100g. However, this increase occurred because the in-flight driving was located in an area close to the monopile. This is why for larger horizontal loading mobilizing the soil faraway, the difference in the soil reaction decreased.

4.3 Quantitative comparison

In addition to the above qualitative comparisons, the effect of impact-driven installation on the lateral response of the monopile was also determined based on two criteria. The first, θ_G = 0.5°, was close to the limit state requirement of serviceability for a typical offshore wind turbine (DNVGL, 2016). The second criterion, $y = 0.1D$ for different soil layers*,* represents the 'ultimate limit state' corresponding to the conventional failure generally admitted for large displacements.

Table 4 summarises, for both tests, the secant stiffness defined at $\theta_G = 0.5°$ for global curves (M_G-θ_G and H_G-y_G/D in Figure 6) and local curves (p-y/D in Figure 10). For both global and local analyses, the installation technique had a significant effect on the secant stiffness: multiplication by 1.6 to 3 for 100*g* driving instead of 1*g* jacking.

The lateral resistances mobilised at $y = 0.1D$ are presented in Table 5. At the ground level, the in-flight installation improved the lateral capacities (H_G and M_G) by 1.45, slightly higher than that reported by Fan *et al.* (2019), who obtained a value of 1.31 for a 3.1*D* embedding into dry sand with a relative density of 38% and $l_e = 3.8\ D$. With regard to the local response of the monopile at 0.1*D* in each layer, the soil reaction increased by 1.24 to 1.33. The in-flight installation improved the soil reaction in deeper layers more significantly, but the effects of in-flight impact driving were pronounced close to the monopile axis for a narrow range of horizontal displacement.

Comparisons of the secant stiffness at $\theta_G = 0.5°$ between the experimental p-y/D curves K_{py}^{exp} and those obtained from the standards K_{py}^{DNVGL} (DNVGL, 2016) are shown in Table 6. This standard suggests an initial modulus of subgrade reaction of about 34 MN/m^3 at a frictional angle of 38°. The experimental stiffnesses were lower than those predicted by the standards. This phenomenon was more pronounced in deeper layers. However, with the in-flight impact driving of the monopile, the results of the experiments were much closer to the standard. Therefore, the lack of stiffness observed in centrifuge modelling was related to the effect of installation and the use of clean, poured sand, which is different form the geological sand used in situ. The DNVGL (2016) yielded results about 2.6 to 5.8 times higher for the J1g test, while for ID100g, the DNVGL values were 1.2 to 2.8 times higher than the experimental ones.

For a large amplitude in case of a normalised displacement of 0.1*D*, the DNVGL-mobilised lateral resistances p^{DNVGL} were compared with those obtained from the experimental *p*-*y*/*D* curves p^{exp} (Table 7). The results show that the experimental lateral resistances were similar to those of the standards. For J1g, the DNVGL resistances were about 1.2 times higher, while for ID100g, the standards resistances were slightly lower than the experimental results.

5 Conclusions

The set-up developed at the Gustave Eiffel University allows for the combination of the impact-driven installation of a 50 mm monopile with a new miniature electro-mechanical hammer, followed by horizontal monotonic loading in a centrifuge at 100*g*.

The global and local horizontal responses of the monopile were investigated for two methods of installation—impact driving at 100*g,* and monotonically jacked installation at 1*g*—into water-saturated Fontainebleau NE34 sand up to a depth of 5 *D*. No soil plugging was observed, which enables an accurate comparison of the responses of the monopile under lateral loading. The findings are as follows:

- A set of two diametrically opposed FBGs, which measured normal strains within the monopile, resisted the driving process at 100*g*. The optical fibres worked appropriately in the subsequent lateral load tests. The bending moment calculated by using the force of the horizontal actuator was in accordance with that measured by the FBGs at the ground level.
- During horizontal loading, the compressive and tensile normal strains were asymmetric, as has been reported by Li *et al*. (2020). Furthermore, the asymmetry was more significant at the monopile base. This might have occurred due to strain localisation at the boundaries of the monopile, as its slenderness ratio was too low to consider it to be a flexible beam.
- The driven monopile better resisted overturning moments and forces, especially in case of small loading amplitude. This enhancement decreased progressively as the resistance increased until it stabilised at high loading amplitudes. These findings have also been reported by Fan *et al*. (2019).

- With regard to serviceability conditions ($\theta_G \leq 0.5°$), the increase in secant stiffness was highly pronounced in case of in-flight driving installation (3 times greater than in case of the 1*g* installation).
- In case of the ultimate state condition (y/D ~ 0.1), an increase in the lateral capacity of the in-flight driving installation was prominent (1.3 times higher).
- The effect of impact driving was more localised in the vicinity of the monopile, and was more pronounced for a narrow range of horizontal displacement. This may be owing to the strong radial stress state induced during impact driving that was not present far from the monopile.
- The DNVGL (2016) predicted stiffness value 2.6 to 5.8 times higher than the experimental ones for the J1g test. For the ID100g test, the DNVGL values were 1.2 to 2.8 times higher.
- The ultimate resistance values of the DNVGL were similar to the experimentally mobilised capacities for normalised displacement of 0.1*D* at a large amplitude.

Developing an electro-mechanical hammer requires ingenuity, time, and validation of the relevant concepts from 1*g* progressively up to 100*g*. Nevertheless, it is important to model impact-driven installation in the centrifuge as it clearly stiffens the soil–monopile interaction.

In future work, the authors will consider the effects of the embedding depth, the use of fluid with scaled viscosity, and the blow rate on the lateral response of impact-driven monopiles.

Acknowledgements

This research study received state support from the National Research Agency under the Investments for the Future Program (ANR-10-IEED-0006-08), and from the France Energies Marines (SOLCYP+) and the Weamec (West Atlantic Marine Energy Community) through the REDENV-EOL project. The authors thank Gustave Eiffel University and the Region Pays de la Loire for financial support in the form of thesis grants. Finally, we are grateful to the centrifuge team at Gustave Eiffel University (Stéphane Lerat, Alexandre Jagu, Patrick Gaudicheau, Alain Néel, and Philippe Audrain) for their technical support in building the experimental device.

References

Abadie CN, Byrne BW and Houlsby GT (2019) Rigid pile response to cyclic lateral loading:

laboratory tests. *Géotechnique*, ***69*(10):** 863–876, https://doi.org/10.1680/jgeot.16.P.325.

API (American Petroleum Institute) (2007) *API RP 2A-WSD: Recommended Practice for Planning, Designing and Constructing Fixed Offshore Platforms - Working Stress Design.* API, Washington, DC, USA.

Astley RJ (1992) *Finite Elements in Solids and Structures: An introduction*. Chapman & Hall, London, UK.

Bayton SM, and Black JA (2016) The effect of soil density on offshore wind turbine monopile foundation performance. In *Proceedings of 3^{rd} European Conference on Physical Modelling in Geotechnics,* Eurofuge, Nantes (Thorel L, Bretschneider A, Blanc M and Escoffier S (eds)). IFSTTAR, Nantes, France, pp. 239–244. See https://www.issmge.org/uploads/publications/53/54/036-bayton%20&%20Black.pdf (accessed 01/06/2016).

Burd HJ, Beuckelaers WJAP, Byrne BW *et al*. (2020a) New data analysis methods for instrumented medium-scale monopile field tests. *Géotechnique,* **70(11):** 961–969, https://doi.org/10.1680/jgeot.18.pisa.002

Burd HJ, Taborda DM, Zdravković L *et al.* (2020b) PISA design model for monopiles for offshore wind turbines: application to a marine sand. *Géotechnique*, **70(11):** 1048–1066, https://doi.org/10.1680/jgeot.18.P.277.

Byrne BW, McAdam RA, Burd HJ *et al.* (2017) PISA: New design methods for offshore wind turbine monopiles. In *Offshore Site Investigation and Geotechnics (OSIG) – Smarter solutions for Future Offshore Developments: Proceedings of the 8^{th} International Conference*. Society for Underwater Technology, London, UK, vol. 1, pp. 142–161.

Byrne BW, McAdam RA, Burd HJ *et al.* (2020) Monotonic laterally loaded pile testing in a stiff glacial clay till at Cowden. *Géotechnique,* **70(11):** 1030–1047, https://doi.org/10.1680/jgeot.18.P.255.

Choo YW, and Kim D (2016) Experimental development of the p-y relationship for large-diameter offshore monopiles in sands: Centrifuge tests. *Journal of Geotechnical and Geoenvironmental Engineering*, **142(1)**: 04015058, https://doi.org/10.1061/(ASCE)GT.1943-5606.0001373.

De Nicola A (1996) *The performance of Pipe piles in sand. Doctoral dissertation, University of*

Western Australia, Perth, Australia.

De Nicola A and Randolph MF (1994) Development of a miniature pile driving actuator. In *Centrifuge 94: Proceedings of the International Conference Centrifuge 94 (*Leung CF, Lee FH and Tan TS (eds)). Balkema, Rotterdam, the Netherlands, pp. 473–478.

De Nicola A and Randolph MF (1997) The plugging behavior of driven and jacked piles in sand. *Geotechnique*, ***47*(4)**: 841–856, https://doi.org/10.1680/geot.1997.47.4.841.

DNVGL (Det Norske Veritas and Germanischer Lloyd) (2016) *Standard DNVGL-ST-0126: Support structures for wind turbines, April 2016*. DNVGL, Hoevik, Norway.

Doherty P, Igoe D, Murphy G *et al*. (2015) Field validation of fibre bragg grating sensors for measuring strain on driven steel piles. *Geotechnique Letters*, ***5*(2)**: 74–79, https://doi.org/10.1680/geolett.14.00120.

Dupla JC, Palix E, Damblans G *et al*. (2019) The ANR SOLCYP+ project for improving the design of monopiles used as offshore wind turbines foundations. *Revue Française de Géotechnique*, 158: article 4, https://doi.org/10.1051/geotech/2019010 (in french).

Dyson GJ and Randolph MF (2001) Monotonic Lateral Loading of Piles in Calcareous Sand. *Journal of Geotechnical and Geoenvironmental Engineering*, **127(4)**: 346–352, https://doi.org/10.1061/(ASCE)1090-0241(2001)127:4(346).

El Haffar I (2018) *Physical modeling and study of the behavior of deep foundations of offshore wind turbines*. Doctoral dissertation, Ecole Centrale de Nantes, Nantes, France. See https://www.theses.fr/2018ECDN0021 (accessed 01/01/2020).

Faghidian SA (2017) Unified formulations of the shear coefficients in Timoshenko beam theory. *Journal of Engineering Mechanics*, **143(9)**: 06017013, https://doi.org/10.1680/jphmg.18.00028.

Fan S, Bienen B and Randolph MF (2019) Centrifuge study on effect of installation method on lateral response of monopiles in sand. *International Journal of Physical Modelling in Geotechnics* **21(1):** 40–52. https://doi.org/10.1680/jphmg.19.00013.

Fan S, Bienen B, and Randolph MF (2021a) Effects of Monopile Installation on Subsequent Lateral Response in Sand. I: Pile Installation. *Journal of Geotechnical and Geoenvironmental Engineering*, **147(5)**: 04021021, https://doi.org/10.1061/(ASCE)GT.1943-5606.0002467.

Fan S, Bienen B and Randolph MF (2021b) Effects of Monopile Installation on Subsequent Lateral Response in Sand. II: Lateral Loading. Journal of Geotechnical and Geoenvironmental Engineering, **147(5)**: 04021022. https://doi.org/10.1061/(ASCE)GT.1943-5606.0002504.

Garnier J (2001) Physical models in geotechnics. *Revue Française de Géotechnique*, *97*: pp. 3–29. https://doi.org/10.1051/geotech/2001097003 (in french).

Garnier J and Konig D (1998) Scale effects in piles and nail loading tests in sand. In *Centrifuge 98: Proceedings of Internbational conference Centrifuge 98* (Kimura T, Kusakabe O and Takemura J (eds)). Balkema, Rotterdam, the Netherlands, vol. 1, pp. 205–210.

Garnier J, Gaudin C, Springman SM *et al.* (2007) Catalogue of scaling laws and similitude questions in geotechnical centrifuge modelling. *International Journal of Physical Modelling in Geotechnics*, ***7*(3)**: 01–23, https://doi.org/10.1680/ijpmg.2007.070301.

Kim BT, Kim NK, Lee WJ and Kim YS (2004) Experimental load-transfer curves of laterally loaded piles in Nak-Dong River sand. *Journal of Geotechnical and Geoenvironmental Engineering*, **130(4)**: 416–425. https://doi.org/10.1061/(ASCE)1090-0241(2004)130:4(416)

Klinkvort RT (2012) Centrifuge modelling of drained lateral pile-soil response - Application for offshore wind turbine support structures. Doctoral dissertation, Technical University of Denmark, Lyngby, Denmark, See https://core.ac.uk/reader/18600667.

Klinkvort RT (2018) *Centrifuge monopile tests in sand. Factual report of laboratory testing.* Norwegian Geotechnical Institute, Oslo, Norway.

Kutter BL (1994) Recent advances in centrifuge modelling of seismic shaking, state-of -the-Art Paper. In *Proceedings of 3rd International Conference on recent advances in Geotechnical Earthquake Engineering and Soil dynamics.* University of Missouri-Rolla, St. Louis, MO, USA, vol. 2, pp. 927–942.

Levacher D, Morice Y, Favraud C and Thorel L (2008) *A review of pile drivers for testing in centrifuge*. In *Journées Nationales Génie Côtier−Génie Civil No. 10 (2018): Sophia Antipolis* (Levacher D and Gaufres P (eds)), pp. 573–584, https://doi.org/10.5150/jngcgc.2008.055-l. Editions Paralia, Centre Français du Littoral, Nantes, France.

Li Z, Thorel L and Blanc M (2020) Using FBGs to estimate the horizontal response of a monopile in a geotechnical centrifuge. *International Journal of Physical Modelling in Geotechnics*, **20(3)**: 164–174, https://doi.org/10.1680/jphmg.19.00022.

Mayall R (2019) *Monopile Response to Scour and Scour Protection*. Doctoral dissertation, University of Oxford, Oxford, UK. See https://ora.ox.ac.uk/objects/uuid:2886ac08-c59e-409d-8d60-6724443d8d1a.

McAdam RA, Byrne BW, Houlsby, GT *et al.* (2020) Monotonic laterally loaded pile testing in a dense marine sand at Dunkirk. *Géotechnique,* **70(11)**: 986–998, https://doi.org/10.1680/jgeot.18.pisa.004

Remaud D (1999) *Piles subjected to lateral loading: Experimental study on group effect*. Doctoral thesis, Ecole Centrale de Nantes, Nantes, France (in French). See https://www.theses.fr/1999NANT2109 (accessed 26/08/2021).

Rosquoet F, Thorel L, Garnier J and Canepa Y (2007) Lateral cyclic loading of sand-installed piles. *Soils and foundations*, **47(5):** 821–832. https://doi.org/10.3208/sandf.47.821.

Sieffert JG and Levacher D (1995) Scale effect analysis of piles driven in centrifuge. *Revue française de géotechnique*, **70**, pp. 55–68. https://doi.org/10.1051/geotech/1995070055 (in French).

Ternet O (1999) *Reconstitution and Characterization of sand Massive: Application to centrifuge and calibration chamber testing (in french).* Doctoral thesis, Université de Caen Normandie, Caen, France (in French). https://www.theses.fr/1999CAEN2061 (accessed 26/08/2021).

Uesugi and Kishida (1986) Frictional resistance at yield bertween dry sand and mild steel. *Soils and Foundations*, **26(4)**: 139–149. https://doi.org/10.3208/sandf1972.26.4_139.

Van Zeban JCB, Azua-Gonzalez C, Alvarez Grima M, Van't Hof C and Askarinejad A (2018) Design and performance of an electro-mechanical pile driving hammer for geo-centrifuge. In *Physical modelling in Geotechnics (ICPMG 2018) (McNamara A, Divall S, Goodey R*, Taylor N, Stallebrass S and Panchal J (eds)). CRC Press/Balkema, London, UK, vol. 1, pp. 469–473.

Table and Figure Captions

Table 1. Recap of hammers of the centrifuge (updated from Levacher *et al.,* 2008).

Table 2. Instrumentation of the experimental device.

Table 3. Geometric and mechanical characteristics of the model monopile.

Table 4. Experimental lateral secant stiffness at θ_G= 0.5°.

Table 5. Experimental lateral resistance at y/D = 0.1.

Table 6. *p*-*y* secant stiffness at θ_G= 0.5°; from the DNVGL (2016).

Table 7. Lateral resistance at y/D = 0.1; from the DNVGL (2016).

Figure 1. Experimental set-up: (a) schematic drawing; (b) photograph in the centrifuge basket.

Figure 2. (a) Monopile-driving hammer and (b) details of the hammering process.

Figure 3. Top-view photograph after lateral loading.

Figure 4. Instrumentation for the monopile: (a) photograph and longitudinal section of the instrumented monopile. (b) transversal section at the level of optical fibres. FBG, fibre Bragg Grating.

Figure 5. Driving curve (number of blows *n*) and cumulative energy (ξ^N and ξ) at the prototype scale plotted against the normalised settlement of the monopile.

Figure 6. At ground-level: (a) the bending moment plotted against rotation (M_G–θ_G), (b) the horizontal load plotted against normalized deflection (H_G–y_G/D), (c) the monopile rotation plotted against normalised displacement (θ_G –y_G/D).

Figure 7. Distribution of normal strains along the monopile for four horizontal loading states corresponding to an increment of 100 MN.m in the ground-level bending moment.

Figure 8. Profiles of deflection, rotation, bending moment, and shear force of the monopile, and the soil reactions for the (a) J1g test and (b) ID100g test. Four cases of loading were considered at the prototype scale: M_G = 100, 200, 300, and 400 MN.m.

Figure 9. Deflection of the monopile above and below the ground level for the (a) J1g test and (b) ID100g test.

Figure 10. Soil reaction plotted against the normalised monopile deflection for (a) J1g and (b) ID100g tests.

Table 1. Recap of hammers of the centrifuge (updated from Levacher et al., 2008).

Hammer type	*L/D*	g-level	Ram mass (g)	Drop height (mm)	Frequency (Hz)	References
Pneumatic	9.4	100	70	0 – 20	20	De Nicola and Randolph (1994)
Electro-magnetic	25	50	40	20	–	Sieffert and Levacher (1995)
Electro-mechanical	2.9	50	220	40 – 55	35	Van Zeban *et al.* (2018)
Pneumatic	3.1	100	50	17	5	Fan *et al.* (2019)

Table 2. Instrumentation of the experimental device.

Sensor name	Location	Range	Linearity
Displacement	Hydraulic actuator	300 mm	0.01%
Displacement	Electro-mechanical actuator	150 mm	0.1%
Vertical laser disp.	Hammer housing	100 mm	0.3%
Potentiometric disp.	Inside the monopile	104 mm	0.1%
2 Horizontal laser disp.	In front of the electric actuator	120 mm	0.1%
Force	Hydraulic actuator	25 kN	0.2%
Force	Electro-mechanical actuator	5 kN	0.75%

Table 3. Geometric and mechanical characteristics of the model monopile.

Parameter	Model
D (m)	0.05
E (GPa)	72.5
EI (N·m^2)	7.7×10^3
G (GPa)	27.2
L (m)	0.25
l (m)	0.525
l_e (m)	0.25
t (m)	0.0025

Table 4. Experimental lateral secant stiffness at θ_G= 0.5°.

Secant Stiffness	***z***	**Units**	**Test**		***Δ* [%]**
			J1g	**ID100g**	
k_{M_θ}	0	MN.m	337	541	**61**
$k_{H\_y/D}$	0	MN	259	553	**114**
$k_{p\_y/D}$	*0.5D*	MN/m	30	90	**197**
	1*D*	MN/m	65	198	**204**
	1.5*D*	MN/m	105	327	**211**
	2D	MN/m	151	482	**219**
	2.5D	MN/m	204	656	**222**
	3D	MN/m	266	824	**210**

Table 5. Experimental lateral resistance at $y/D = 0.1$.

Load/reaction	***z***	**Units**	**Test**		**Δ [%]**
			J1g	**ID100g**	
M_G	0	MN.m	355	515	**45**
H_G	0	MN	14.2	20.6	**45**
p	0.5*D*	MN/m	1.48	1.84	**24**
	1*D*	MN/m	3.11	3.97	**27**
	1.5*D*	MN/m	4.81	6.32	**32**
	2*D*	MN/m	6.57	8.75	**33**

Table 6. *p-y* secant stiffness at θ_G= 0.5°; from the DNVGL (2016).

z	K_{py}^{DNVGL} (MN/m)		$K_{py}^{DNVGL} / K_{py}^{exp}$	
	J1g	**ID100g**	**J1g**	**ID100g**
0.5D	79	112	2.6	1.2
1*D*	214	324	3.3	1.6
1.5*D*	406	649	3.9	2.0
2D	647	1077	4.3	2.2
2.5 D	907	1566	4.4	2.4
3D	1539	2310	5.8	2.8

Table 7. Lateral resistance at y/D = 0.1; from the DNVGL (2016).

z	p^{DNVGL} (MN/m)		p^{DNVGL} / p^{exp}	
	J1g	**ID100g**	**J1g**	**ID100g**
0.5D	1.74	1.74	1.2	0.9
1*D*	3.85	3.85	1.2	1.0
1.5*D*	5.85	5.85	1.2	0.9
2D	7.23	7.23	1.1	0.8

Figure 1. Experimental set-up: (a) schematic drawing; (b) photograph in the centrifuge basket.

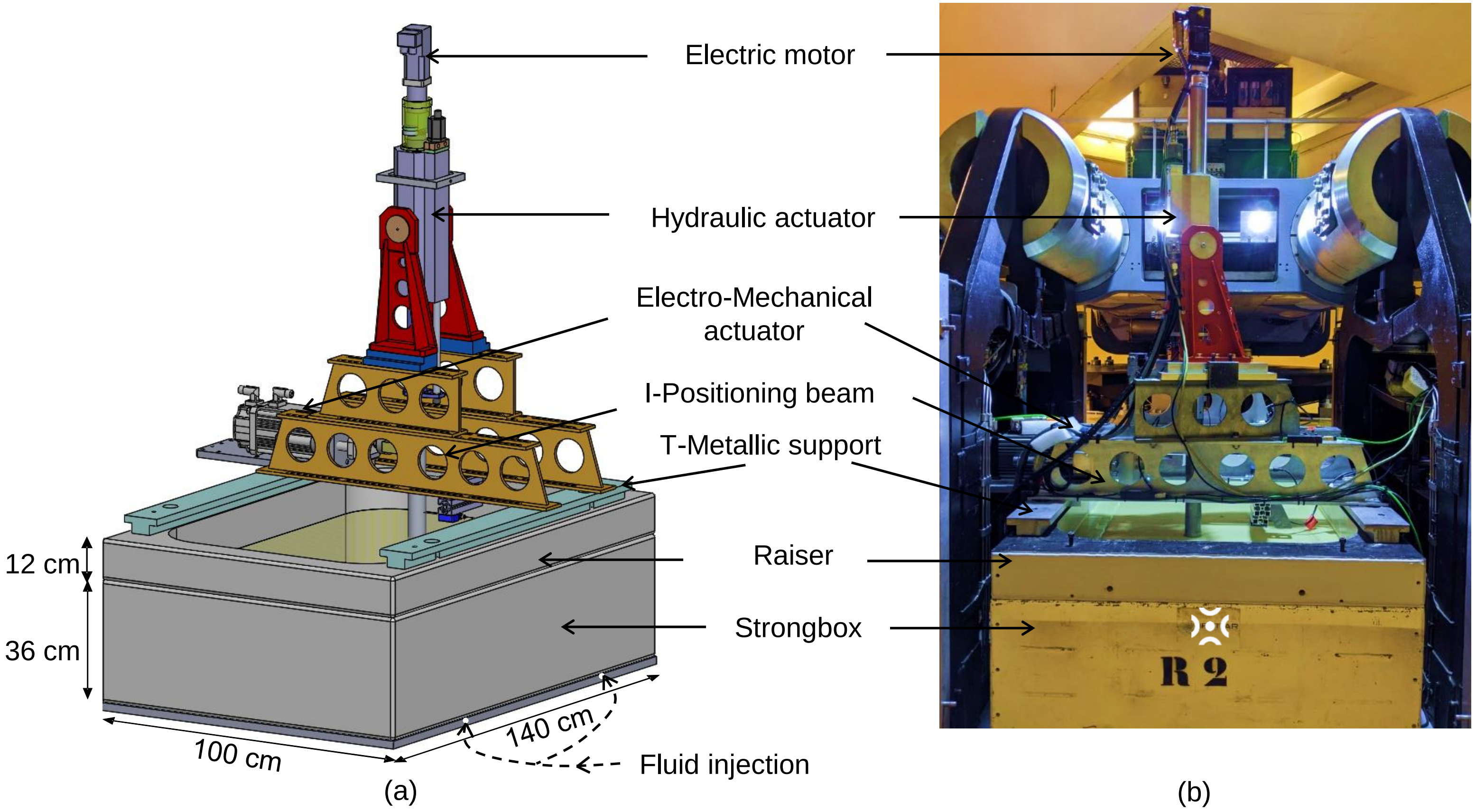

Figure 2. (a) Monopile-driving hammer and (b) details of the hammering process.

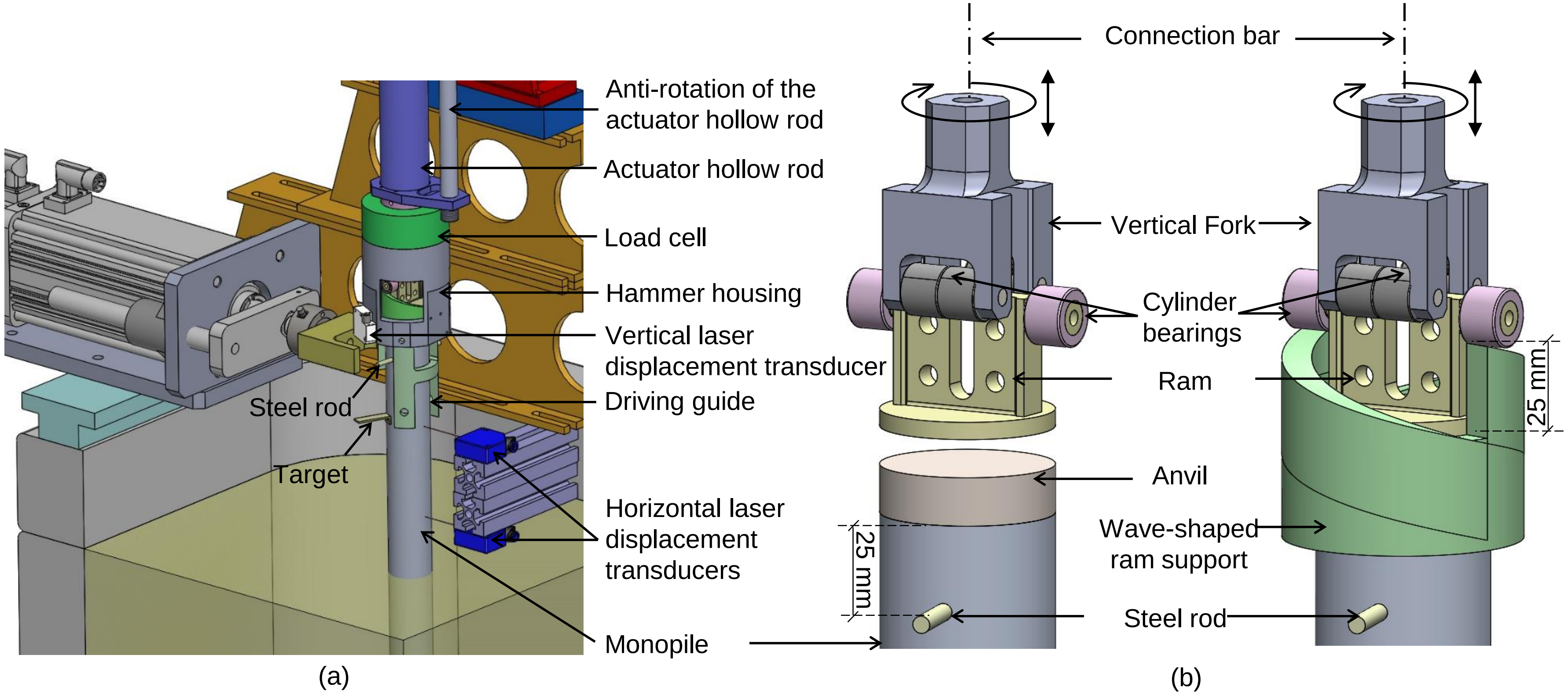

Figure 3. Top-view photograph after lateral loading.

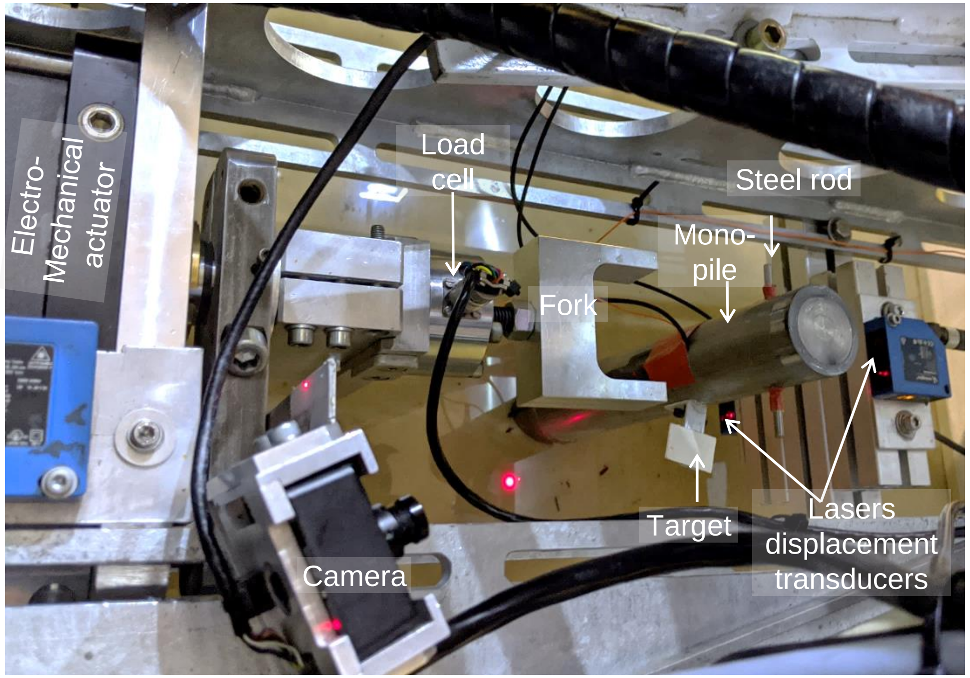

Figure 4. Instrumentation for the monopile: (a) photograph and longitudinal section of the instrumented monopile; (b) transversal section at the level of optical fibres. FBG, fibre Bragg Grating

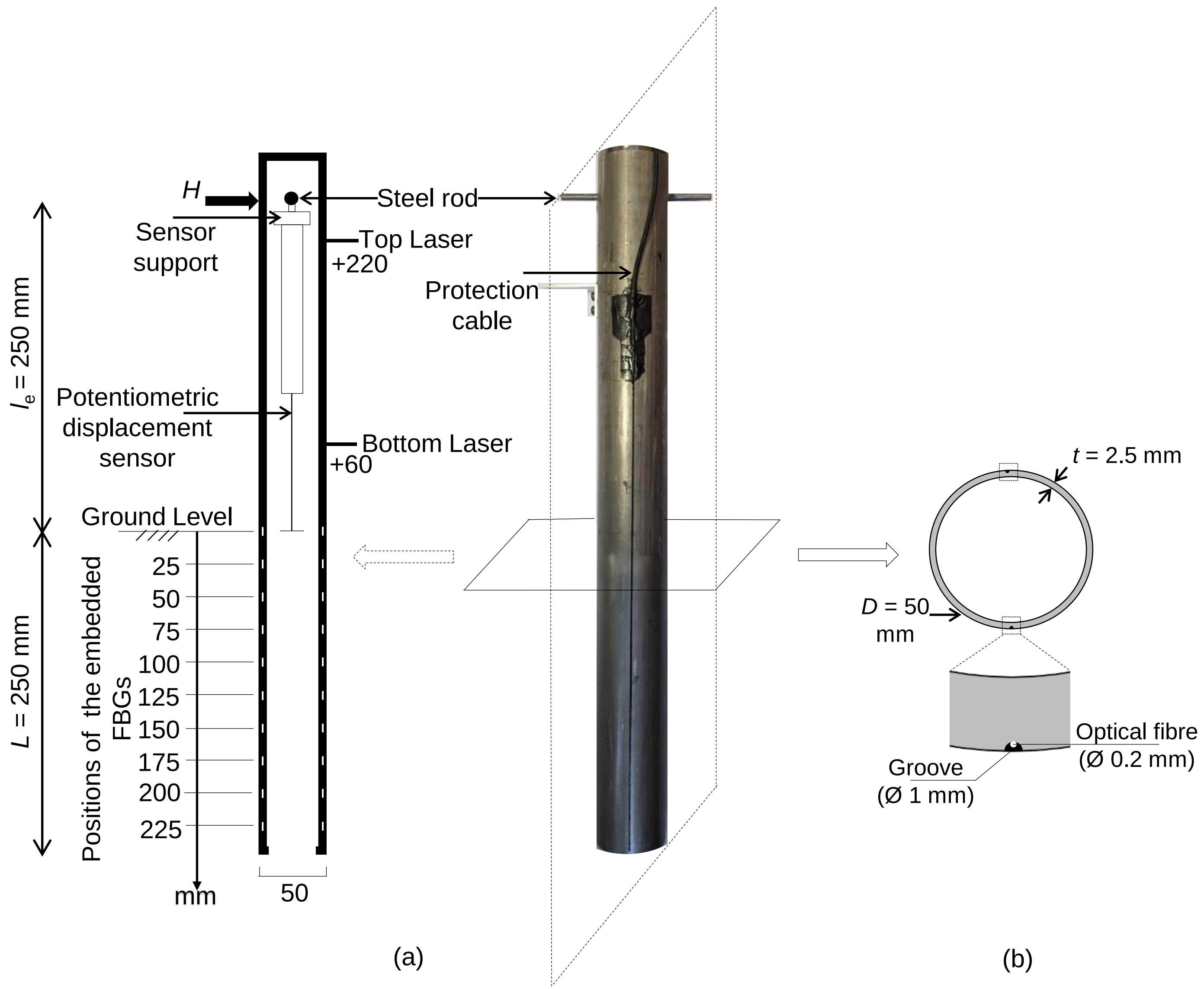

Figure 5. Driving curve (number of blows n) and cumulative energy (ξ^N and ξ) at the prototype scale plotted against the normalised settlement of the monopile.

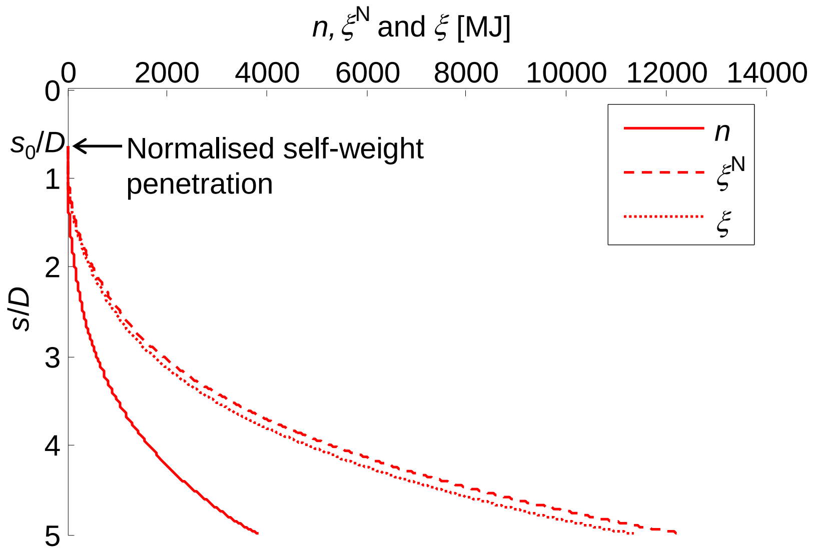

Figure 6. At ground-level: (a) the bending moment plotted against rotation (M_G–θ_G), (b) the horizontal load plotted against normalized deflection (H_G–y_G/D), (c) the monopile rotation plotted against normalised displacement (θ_G–y_G/D).

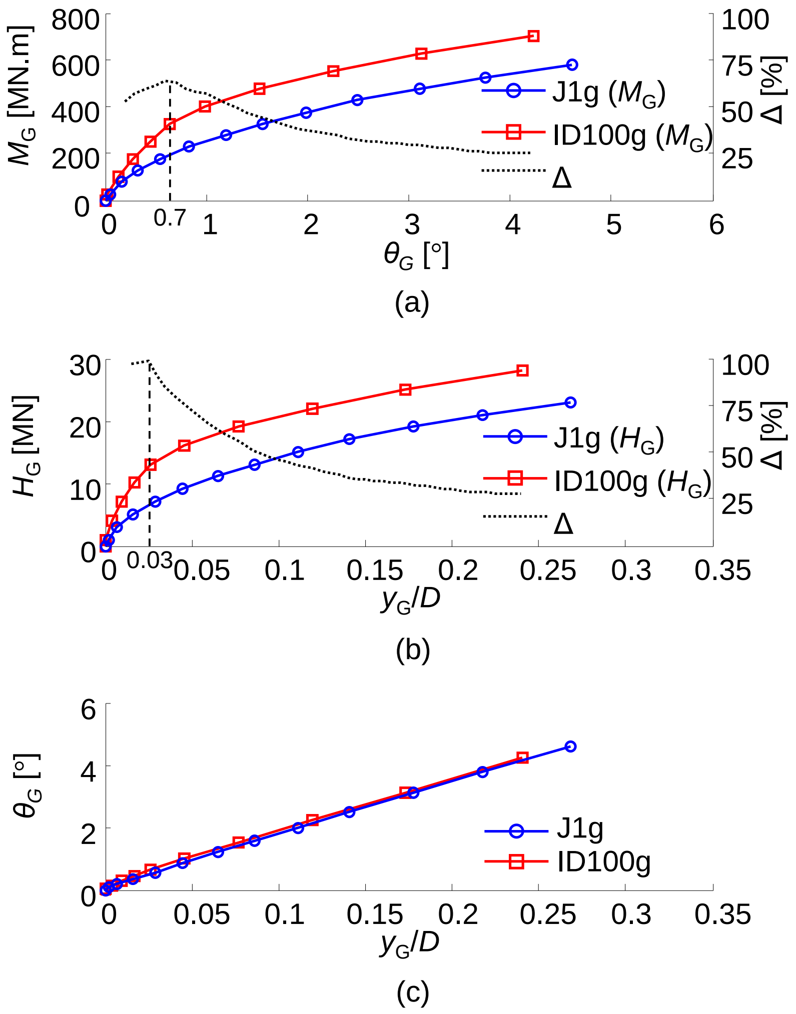

Figure 7. Distribution of normal strains along the monopile for four horizontal loading states corresponding to an increment of 100 MN.m in the ground-level bending moment.

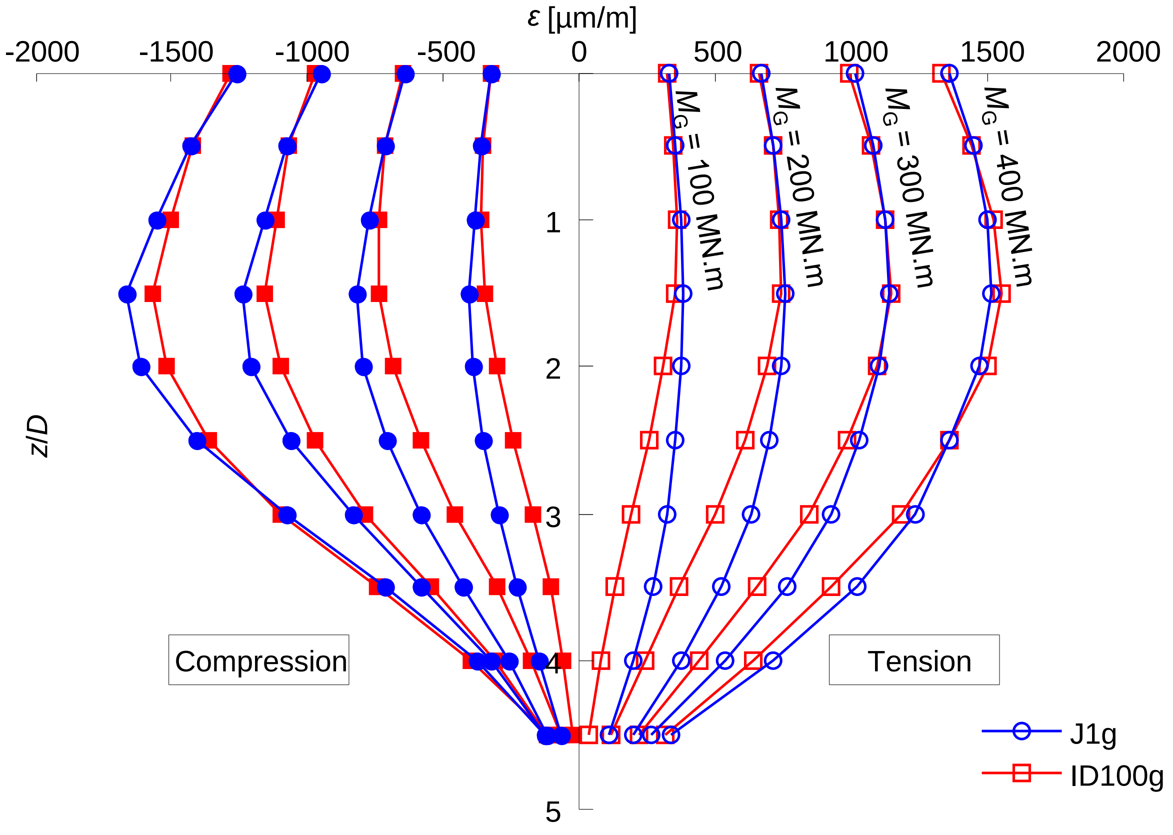

Figure 8. Profiles of deflection, rotation, bending moment, and shear force of the monopile, and the soil reactions for the (a) J1g test and (b) ID100g test. Four cases of loading were considered at the prototype scale: M_G = 100, 200, 300, and 400 MN.m.

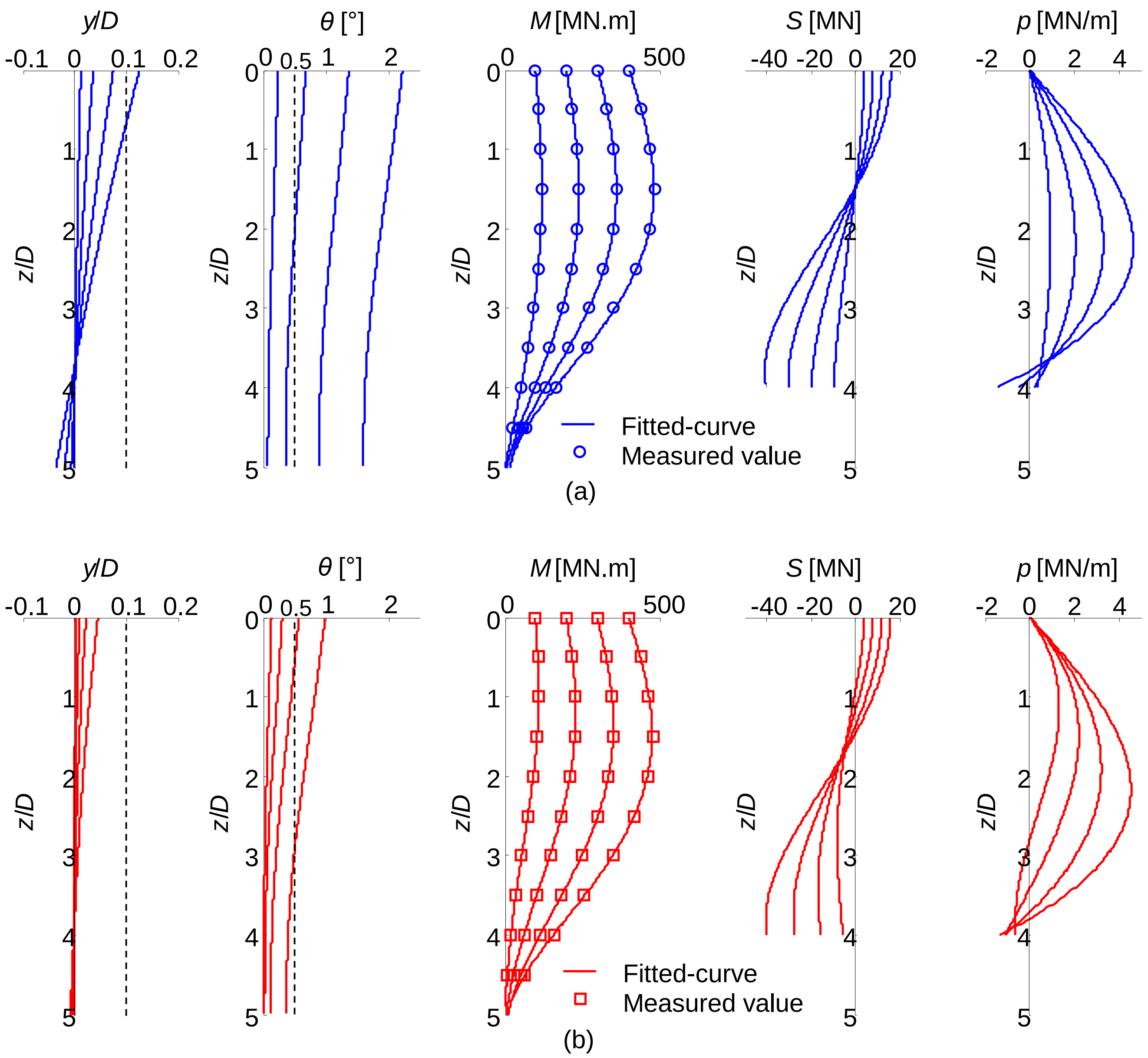

Figure 9. Deflection of the monopile above and below the ground level for the (a) J1g test and (b) ID100g test.

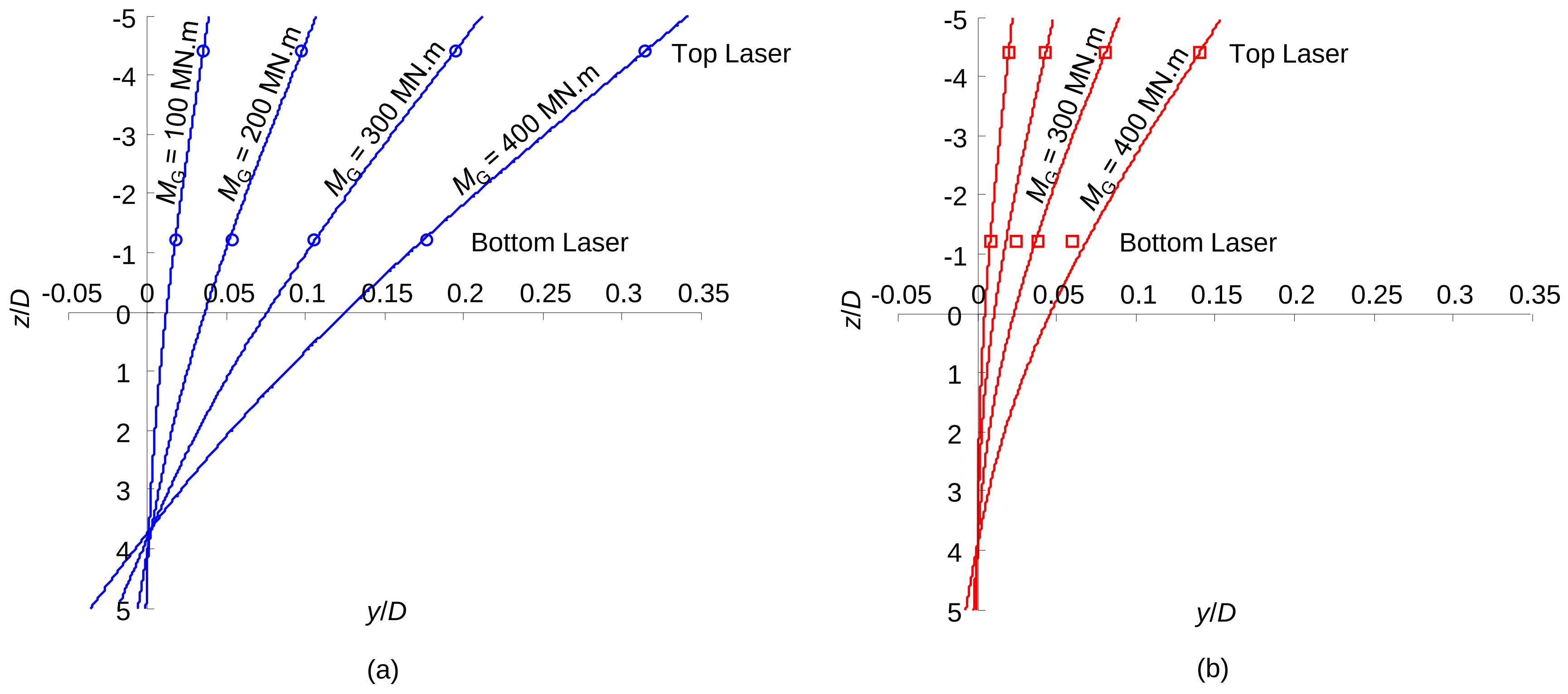

Figure 10. Soil reaction plotted against the normalised monopile deflection for (a) J1g and (b) ID100g tests.